Available online at www.sciencedirect.com
ScienceDirect
Journal of the European Ceramic Society 31 (2011) 507–516
www.elsevier.com/locate/jeurceramsoc

Phase and microstructural evolution of yttrium-doped nanocrystalline alumina: A contribution of advanced microscopy techniques

Paola Palmero [a,*], Claude Esnouf [b]

[a] Dept. of Materials Science and Chemical Engineering, INSTM-R.U. PoliTO, LINCE Lab., Politecnico di Torino, Corso Duca degli Abruzzi 24, 10129 Torino, Italy
[b] Université de Lyon, INSA-Lyon, MATEIS CNRS UMR 5510, 20 Avenue Albert Einstein, F-69621 Villeurbanne, France

Received 3 June 2010; received in revised form 15 October 2010; accepted 30 October 2010
Available online 14 December 2010

Abstract

Well-dispersed nano-crystalline transition alumina suspensions were mixed with yttrium chloride aqueous solutions, with the aim of producing Al_2O_3–$Y_3Al_5O_{12}$ (YAG) composite powders. DTA analysis allowed to highlight the role of yttrium on the α-phase crystallization path. Systematic XRD and HRTEM analyses were carried out in parallel on powders calcined in a wide temperature range (600–1300 °C) in order to follow phase and microstructural evolution. A thin, homogeneous yttrium-rich layer was yielded on the alumina particles surface; yttrium diffusion into the alumina matrix was negligible up to 1150 °C whereas, starting from 1200 °C, aggregates of partially sintered alumina particles appeared, stuck together by yttrium-rich thin films. Moreover, in the yttrium-richer zones, such as alumina grain boundaries and triple joints, yttrium-aluminates precipitated at alumina particles surface. Finally, at 1300 °C, alumina–YAG composite powders were produced, in which YAG was homogenously distributed among the alumina grains.

Keywords: Al_2O_3; Yttrium-doping; Powders-solid state reaction; Electron microscopy; Microstructure-prefiring

1. Introduction

Several oxide impurities, including MgO, CaO, SiO_2, TiO_2, ZrO_2, La_2O_3 and Y_2O_3 play a major role in modifying the microstructure and related properties of sintered polycrystalline α-alumina.[1–3] In addition, small contents (in the range 100–1000 ppm) of various metal cations can lead to an increase of alumina creep temperature and stress limits. Among them, the most effective ones seem to be the trivalent cations, such as yttrium: in fact, due to their ionic radius larger than the aluminium one, they segregate at alumina grain boundary and reduce the intergranular diffusion.[4–6] Moreover, if yttrium content increases up to saturation,[7] $Y_3Al_5O_{12}$ (YAG) precipitation at alumina grain boundaries occurs and dramatically improves both room and high-temperature mechanical properties of the matrix.[8–12]

By keeping in mind the several beneficial effects of YAG on the fired microstructure and on the overall mechanical behavior of alumina, in some previous works[13,14] we have set-up an innovative and easy process for the production of alumina–YAG nanocomposites. Briefly, it consists on the alumina surface modification with an inorganic yttrium salt; upon heating, a highly pure alumina–YAG composite powder is successfully yielded through a solid-state reaction between the yttrium-rich precursor layer and alumina. By strictly controlling all the processing parameters, completely homogenous and fully dense alumina–5 vol.% YAG composite materials were finally obtained. However, a suitable microstructural tailoring of the dense composites can be achieved only through an effective control of the powder features and of the role of its thermal pre-treatment prior forming and sintering.

This paper is therefore aimed to deepen the role of such yttrium-rich precursor on the phase and microstructural development of a nanocrystalline transition alumina powder, upon thermal treatment. In particular, we used advanced microscopy techniques (such as HRTEM and HAADF) to follow the whole path from the starting alumina surface doping to the final development of the composite powder. In fact, to the best of the

* Corresponding author. Tel.: +39 011 5644678; fax: +39 011 5644688.
E-mail addresses: paola.palmero@polito.it (P. Palmero), claude.esnouf@insa-lyon.fr (C. Esnouf).

0955-2219/$ – see front matter © 2010 Elsevier Ltd. All rights reserved.
doi:10.1016/j.jeurceramsoc.2010.10.037

Author's knowledge, a similar systematic investigation was never reported in literature, even for alumina–YAG composite materials yielded by quite similar doping process.[2,9,15]

A deeper understanding of the crystallization mechanism and microstructural evolution phenomena involved is the second goal which aims this work. In fact, if achieved, it can supply some general guidelines of this quite innovative processing route, leading to its more conscious exploitation toward the production of a wide range of micro/nanocomposites materials, having controlled and homogeneous microstructures.

2. Experimental

A commercial, nano-crystalline alumina (Nanotek®, supplied by Nanophase Technologies Corporation, Darien, IL, USA), produced by a physical vapour synthesis (PVS) process, was used as starting material. The powder has a spherical morphology, is highly pure (99.95%) with an average crystallites size of 45 nm and a specific surface area of 35 $m^2\ g^{-1}$. It is composed by γ/δ-transition alumina phases, as declared by the supplier,[16] even if the δ*-Al_2O_3 phase [ICDDP file no. 46-1215] was also detected, as described in a previous paper.[17] From literature,[18] the δ*-Al_2O_3 phase is formed during the phase transformation from γ to α-alumina in plasma treated materials.

Nanotek® powder was dispersed in distilled water under magnetic stirring for 120 h, reaching an average particle agglomerate size of about 0.5 μm.[17]

Aqueous solutions of $YCl_3{\cdot}6H_2O$ (Aldrich, 99.99% purity) were employed as yttrium precursor for developing alumina–$Y_3Al_5O_{12}$ (YAG) composites, containing 5 (AY-5), 10 (AY-10) and 20 (AY-20) vol.% YAG. Further details on this process can be found elsewhere.[13,14] The yttrium-doped slurries were kept under magnetic stirring for two additional hours and then dried in an oven at 105 °C.

The doped powders were characterized as follows:

- DTA–TG analysis (Netzsch STA 409C), performed on powdered samples of about 150 mg, up to 1450 °C in static air, at a heating rate of 10 °C/min. On the ground of thermogravimetric results, powders were calcined at 600 °C for 6 min, at 900 °C, 1150°, 1200 °C, 1300 °C and 1500 °C for 30 min, at a heating and cooling rate of 10 °C/min, in air.
- X-ray diffraction (XRD) analysis (Philips PW 1710), performed on the same calcined powders. Cu Kα radiation (1.541874 Å) was used; spectra were acquired in the range 5–70° 2θ, with a step size of 0.05° 2θ and an acquisition time per step of 5 s. Diffraction patterns were indexed by using the Powder Data File database (P.D.F. 2000, International Centre of Diffraction Data, Pennsylvania).
- High resolution transmission electron microscopy (HRTEM) observations performed by a JEOL 2010 FEG instrument operating at 200 kV; elemental analyses were performed by energy dispersive X-ray spectroscopy (EDX INCA system) under a nano-probe condition (beam size in the range 2–5 nm). Some micrographs were also obtained using a chemical information mode with an high angle annular dark field detector (HAADF), sensitive to the atomic number variations (Z contrast). The analyses were carried out on the doped powders just dried at 105 °C or calcined in the 600–1300 °C temperature range. Powders were ultrasonically dispersed into absolute ethanol; the suspensions were deposited on a holey carbon film and then let to dry at ambient conditions.

3. Results

3.1. DTA–TG analysis

TG analyses of the three doped materials evidenced that the by-products (mainly chlorides) decomposition was almost accomplished at about 450 °C. Upon heating, AY-5, AY-10 and AY-20 underwent to total mass loss of 6.6, 14.7 and 20.8%, respectively.

DTA curves allowed to evidence the metastable (precisely, the θ-phase[19]) to α-Al_2O_3 transformation temperature; this value is reported in Fig. 1 as a function of the YAG volume fraction, showing an exponential increase of such temperature by increasing the yttrium content. For sake of comparison, the α-Al_2O_3 crystallization temperature in raw Nanotek® was also evaluated, showing the lowest value.

In AY-20, two additional DTA signals at about 900 °C and 1075 °C were also detected: as discussed in the following, the former exothermic peak can be imputed to the crystallization of the monoclinic $Al_2Y_4O_9$ (YAM), the latter to its conversion into aluminium-richer phases, such as YAG and/or hexagonal $YAlO_3$ (h-$YAlO_3$). In contrast, AY-5 and AY-10 DTA curves showed only the α-alumina exothermal crystallization, whereas yttrium-aluminates signals were not visible due to their lower yttrium content.

3.2. XRD analysis

The three doped powders showed different crystallization paths as a function of the calcination temperature: the crystalline phases detected are collected in Table 1.

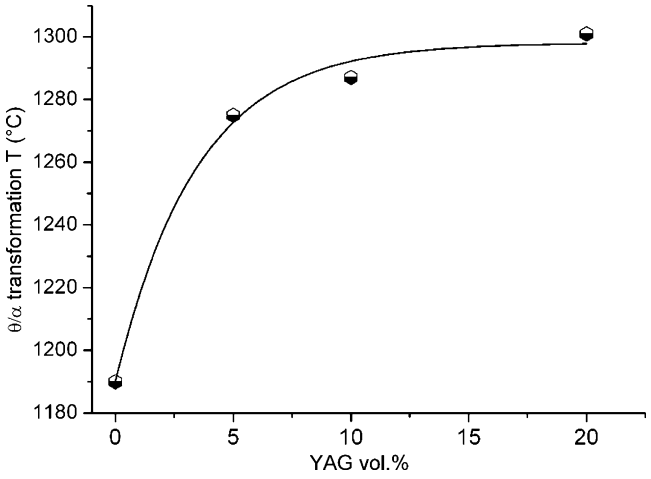

Fig. 1. Metastable to α-Al_2O_3 phase transformation temperature as a function of YAG volume percentage in the composite powders.

Table 1
Phase composition of AY-5, AY-10 and AY-20 by XRD data as a function of the thermal treatment (t = traces).

Thermal treatment	AY-5	AY-10	AY-20
600 °C – 6 min	δ/δ*-Al_2O_3	δ/δ*-Al_2O_3	δ/δ*-Al_2O_3
900 °C – 30 min	δ/δ*-Al_2O_3	δ/δ*-Al_2O_3	δ/δ*-Al_2O_3/YAM (t)
1150 °C – 30 min	δ/δ*-Al_2O_3	δ*-Al_2O_3/YAG	θ/δ*-Al_2O_3/YAG/h-$YAlO_3$
1200 °C – 30 min	θ/α-Al_2O_3/YAG/h-$YAlO_3$	θ/α-Al_2O_3/YAG/h-$YAlO_3$	θ/α-Al_2O_3/YAG/h-$YAlO_3$
1300 °C – 30 min	α-Al_2O_3/YAG/h-$YAlO_3$/YAP (t)	α-Al_2O_3/YAG	α-Al_2O_3/YAG/h-$YAlO_3$ (t)
1500 °C – 30 min	α-Al_2O_3/YAG	α-Al_2O_3/YAG	α-Al_2O_3/YAG

In AY-5, only transition alumina phases were found up to 1150 °C, with an increase in the peaks intensity from 900°C to 1150 °C; α-Al_2O_3 and yttrium-aluminates started to crystallize at 1200 °C with the simultaneous appearance of YAG and h-$YAlO_3$; at 1300 °C, also the orthorhombic perovskite $YAlO_3$ (YAP) was detected. In AY-10, pure YAG was found after calcination at 1150 °C, but at higher temperature (1200 °C), also h-$YAlO_3$ was detected. AY-20 calcined at 900 °C yielded monoclinic $Al_2Y_4O_9$, which corresponds to the yttrium-richer phase in the Al_2O_3–Y_2O_3 system[20]; however, at higher temperatures (1150 °C and 1200 °C), it converted into YAG and h-$YAlO_3$.

Finally, if calcined at even higher temperature (i.e. at 1500 °C for 30 min), only α-Al_2O_3 and YAG phases appeared: consequently, all the aforementioned second-phases can be considered as crystallization intermediates. To better follow the phase development as a function of the composition, Fig. 2 collects the XRD patterns of the three composite powders after calcination at 1200 °C. Almost the same crystalline phases are present (as detailed in Table 1), but the peaks intensities significantly differ. As expected, near the increase of the yttrium-aluminates reflections from AY-5 (curve I) to AY-20 (curve III), an opposite trend is observed for α-Al_2O_3 peaks. The α-Al_2O_3 crystallized fraction (X_α) was evaluated by the ratio A_x/A_{100}, where A_x is the area obtained by integrating the stronger XRD α-peak {1 1 3} at 1200 °C for each material and A_{100} is the respective area for fully crystallised samples (precisely, after calcination at 1500 °C for 30 min). X_α is about 92, 82 and 32% in AY-5, AY-10 and AY-20, respectively, showing an inverse proportion among the yttrium content in the doped powders and the transformed α-alumina fraction.

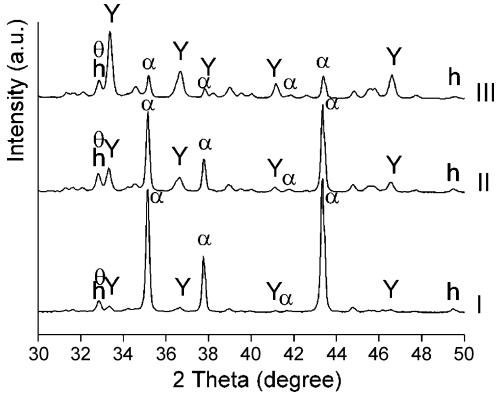

Fig. 2. XRD patterns of AY-5 (I), AY-10 (II) and AY-20 (III) calcined at 1200 °C for 30 min (α = α-Al_2O_3, θ = θ-Al_2O_3, Y = YAG, h = h-$YAlO_3$). For the sake of clarity, only the 30–50° 2θ range is reported.

3.3. HRTEM characterization

HRTEM was carried out on AY-5, thermally treated in a wide temperature range (from as-dried at 105° to the calcined product at 1300 °C). In the followings, the main results of "low"- (105–1150 °C) and "high"- (1200 and 1300 °C) thermal treatments are separately presented, according to the previous XRD data, showing only transition alumina evolution in the former temperature range and α-Al_2O_3 and yttrium-aluminates crystallization in the latter. However, to deepen the discussion on the microstructural development of yttrium-doped alumina powders, some high-temperature calcined AY-10 and AY-20 samples were also characterized and compared to AY-5.

3.3.1. Low-temperature treatments (105–1150 °C)

The spherical morphology, typical of raw NanoTek®,[16] also characterizes the low-temperature treated AY-5 powders. In addition, they appear in form of packets of few primary particles, proving the effectiveness of the performed dispersion process. This feature is shown, as an example, in Fig. 3(a) for AY-5 just-dried at 105 °C. A deeper microstructural insight of the same powder is given in Fig. 3(b): inset to the figure are (i) a higher-magnification of an alumina particle (top-left side) and (ii) its indexed fast Fourier transform (FFT) (top-right side), which allowed the identification of the δ-Al_2O_3 phase. The alignments of closed-packed spots, as the FFT shows, are attributed to a high density of structural defects into the transition alumina lattice. In addition, a slight difference between the alumina bulk and surface is noticed. In fact, the inner part of particles appears to be well crystallized, as evidenced by the diffraction fringes of the atomic planes, whereas the surface is characterized by a less-ordered layer made of few atomic planes. This feature can be attributed to the prolonged dispersion process in aqueous medium, also able to induce modifications of the compositional and physico-chemical surface properties of the transition alumina, as reported in a previous paper.[21] Indeed, a statistical detection of yttrium can be obtained by using an EDX nanoscale probe focused on alumina grains surface; on the contrary, inside the grain, even at few nanometers far from the surface, the dopant concentration was lower than the detection limit. Thus, the doping process is effective in inducing the formation of a very thin, continuous yttrium-enriched layer on the alumina surface. According to this result, it can be assessed that no – or very limited – segregation phenomena of the dopant occur during the drying process of the aqueous alumina suspensions, being this an important requirement to reliably prepare homogeneous alumina–YAG composite materials.[13,14]

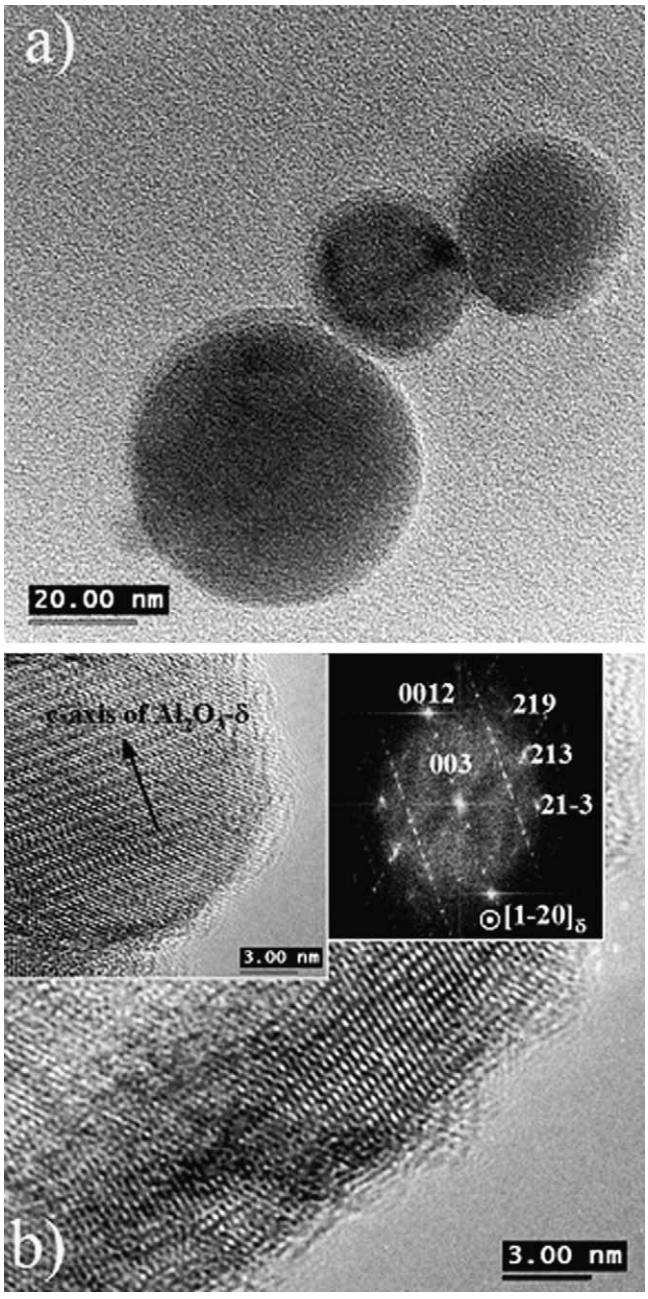

Fig. 3. Lower (a) and higher (b) HRTEM magnifications of as-dried AY-5; inset to the figure (b) a smallest alumina particle (top-left side) and the related indexed FFT (top-right side).

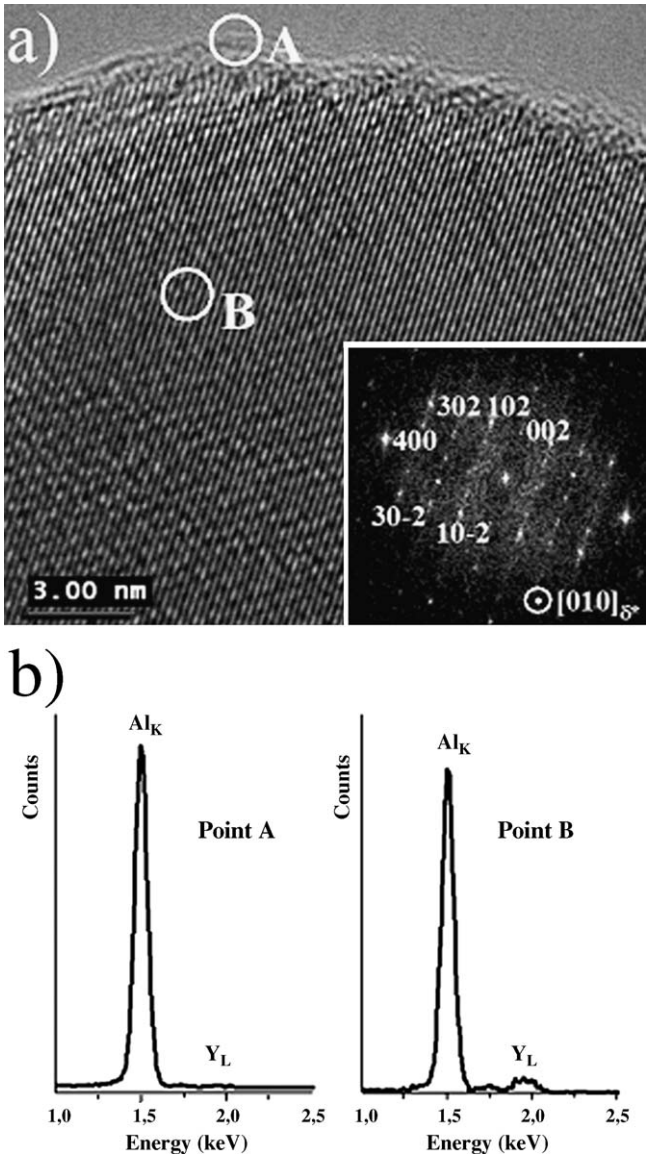

Fig. 4. (a) HRTEM micrograph of AY-5 calcined at 1150 °C; inset to the figure the related indexed FFT. Circles materialize the beam impact during EDX measurements (beam size ~2 nm); (b) EDX peaks of Y and Al in points A and B of figure (a).

Similar features also characterize AY-5 calcined at 600 °C, 900 °C and 1150 °C. The same poorly crystallized, yttrium-rich surface layer was observed on these powders, whereas yttrium was never detected inside the particles (even at few nanometres far form the surface), denoting a negligible yttrium diffusion in the alumina bulk up to 1150 °C. See, for instance, points A and B in Fig. 4(a) for AY-5 calcined at 1150 °C: the relative Y and Al EDX spectra in such points are collected in Fig. 4(b). Moreover, in this temperature range, yttria and/or yttrium-aluminates precipitates were not observed, according to XRD data (see Table 1). For what concerns phase identification, the alumina particle of the high-magnification HRTEM micrograph in Fig. 4(a) was identify as δ*-Al_2O_3, as shown by the relative indexed FFT (inset to the same figure). A deepening on the indexation work of the transition phases of Nanotek® is reported in Section 4. Notice here always a bad-crystallized layer on the periphery of particles.

3.3.2. High-temperature treatments (1200–1300 °C)

Powders calcined in this temperature range firstly experienced a morphological modification. In fact, we observe now aggregates of both rounded-shaped and well-facetted alumina particles, the latter associable to the α-phase which begins to crystallize, as stated by XRD analysis.

This feature is evidenced in the HAADF micrographs of Fig. 5, related to AY-5 (a), AY-10 (b) and AY-20 (c) calcined at 1200 °C. Fig. 5(a) well evidences a large aggregate of partially

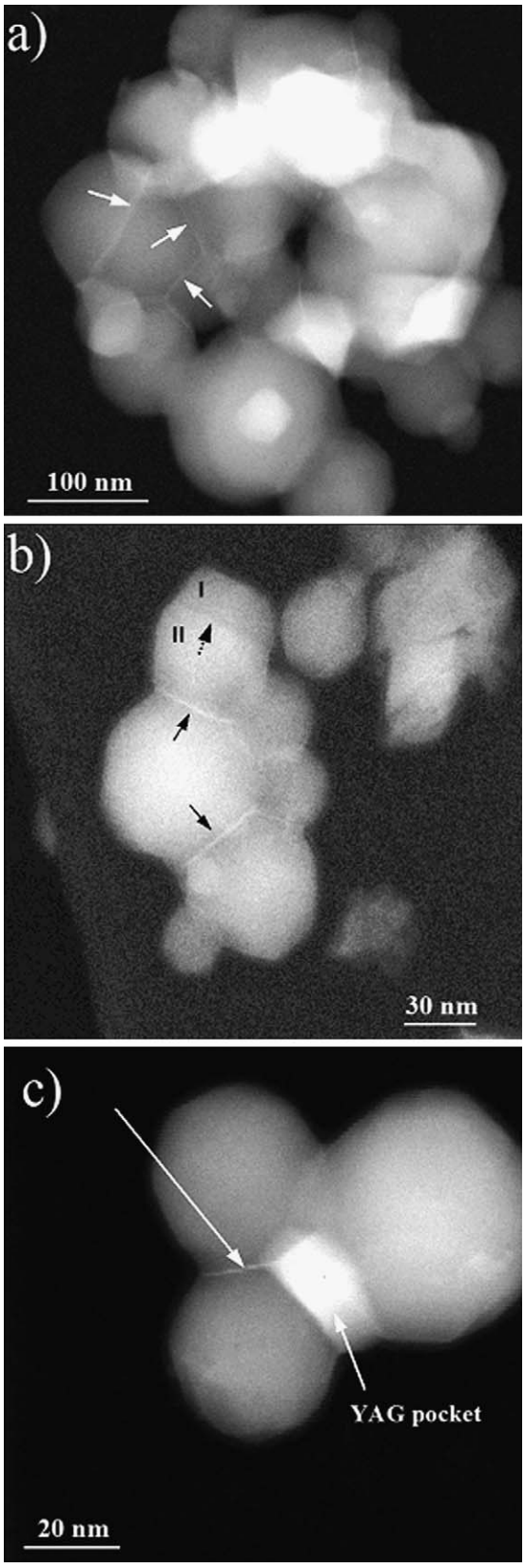

Fig. 5. HAADF micrographs of (a) AY-5, (b) AY-10 and (c) AY-20 calcined at 1200 °C. Solid-line arrows show the yttrium-rich films; the dotted line arrow in figure (b) shows a twin boundary dividing an alumina grain in domains I and II.

sintered alumina particles, entrapping some nanometric pores. In all these images, according with the HAADF contrast, the dark grains can be associated to alumina and the lighter areas to yttrium-rich phases; it is possible to appreciate at the junctions between darker alumina grains the presence of several bright, yttrium-rich thin films (see the solid-line arrows in the three images), "sticking" the alumina grains each other. To confirm the different chemical composition, the EDX nanoprobe was repeatedly focused on these films and then on adjacent regions, at few nanometres far from the bright layers. Remarkable Y signals were recorded on the films, whereas in the neighboring areas, only the Al EDX peak was detected. In AY-5 the mean film thickness was estimated, giving the value of about 1.1 nm.

Under deeper microstructural observations, some structural lattice defects inside alumina particles can be noticed (see, for instance, the dotted-line arrow of Fig. 5(b)), dividing the grain into two domains, here labelled I and II. Contrasting from the previously described yttrium-rich films, these "special" alumina grain boundaries were completely yttrium-free. A higher magnification image of the defect can be found in Fig. 9(a) and a deepening on this peculiar feature is reported in Section 4.

At this temperature, the crystallization of yttrium-aluminates also occurs, in agreement with the previous results by Maglia et al.[22] who reported a decreased solubility of trivalent ions in the corundum structure as compared to the γ-phase and a consequent second-phase precipitation during γ to α-Al_2O_3 transformation. In fact, Fig. 6(a) shows a small crystallite precipitated at alumina surface in AY-5 whereas a small particle located at the interface of two alumina grains is evident in Fig. 6(b) for AY-10. Finally, form the previous Fig. 5(c), we can notice a bright yttrium-rich grain located at a triple joint of three darker alumina grains in AY-20. The phase identification of the crystallite in AY-5 was carried out by exploiting its FFT (inset to the figure) obtained by a higher magnification image; the indexation corresponds to monoclinic YAM (even if undetected by XRD), according to lattice distances and respective angles between lattice planes of JCPDS file no. 83-0933. A clear phase confirmation by means of EDX analysis was not easy: in fact, it supplied a Y/Al atomic ratio for the crystallite of about 0.4, quite different from the expected value of 2. A similar result was found in AY-10: in fact, EDX analysis of point A in Fig. 6(b) supplied a Y/Al atomic ratio of 0.34, in a spare matching with any yttrium-aluminate phase. However, taking into account the ultra-fine size of the above crystallites, a discrepancy in chemical analysis can be reasonably imputed to the surrounding alumina matrix which affects the Al quantification (matrix effect). In spite of this, the EDX spectra superimposed to Fig. 6(b) clearly shows a significant yttrium enrichment in point A, a progressive yttrium depletion on the boundary (points B and C) and a completely yttrium-free surrounding alumina matrix (point D).

Finally, Fig. 7 is a HAADF micrograph of AY-5 calcined at 1300 °C. The increase in temperature induces a partial sintering of the primary particles: as a result, a large aggregate, made by well-distributed light and dark grains and entrapping a diffuse nanosized porosity can be now observed. On the same sample,

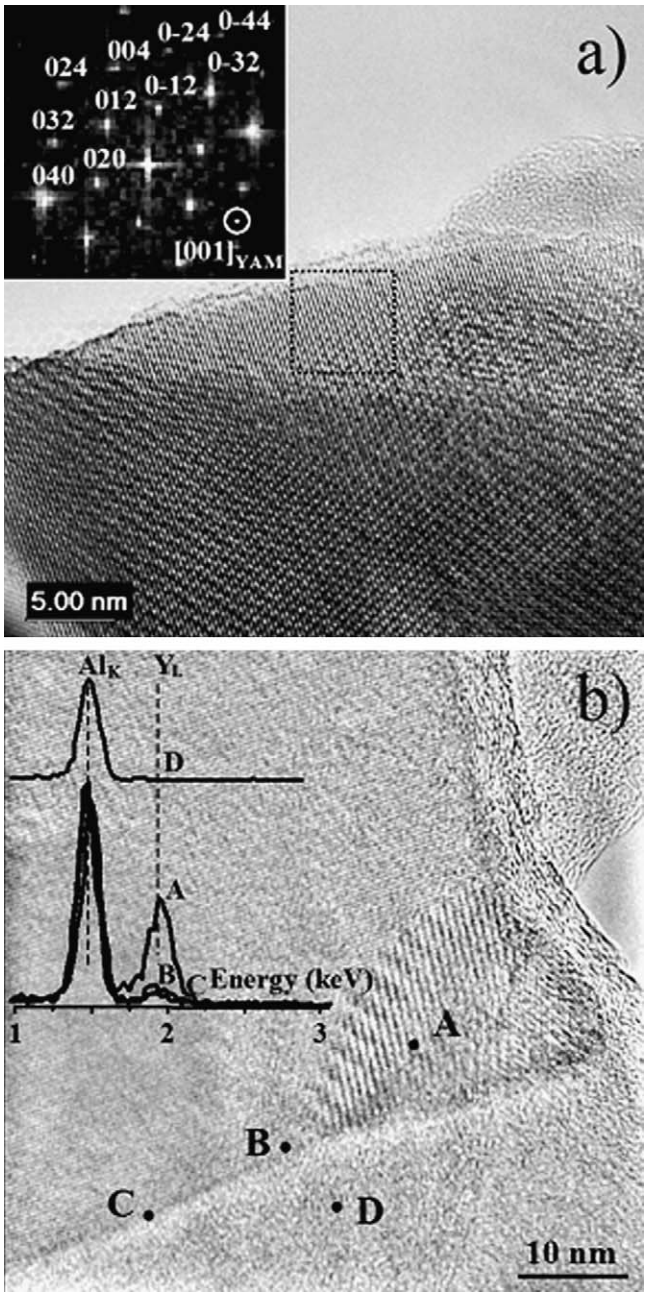

Fig. 6. HRTEM micrographs of (a) AY-5 and (b) AY-10 calcined at 1200 °C. Inset to figure (a) the related indexed FFT. EDX spectra obtained at points A–D of figure (b) are superimposed in the same figure (beam size ~5 nm in A and D, ~2 nm in B and C).

Fig. 8(a) evidences a half-rounded particle growing on the surface of an alumina grain. In this case, both EDX analysis and FFT indexation allowed to associate the second-phase crystallite to YAG phase. In fact, in point A, a Y/Al atomic ratio of 0.6 was found, consistent with the 3:5 molar ratio of garnet-type compound. As a comparison, in the surrounding matrix (point B), yttrium was not detected (EDX peaks at the above points are drawn in Fig. 8(b)). The indexed FFT related to the same crystallite (inset to (a)) confirms the YAG phase, according to the crystallographic parameters given by JCPDS file 33-40 or 01-079-1892.

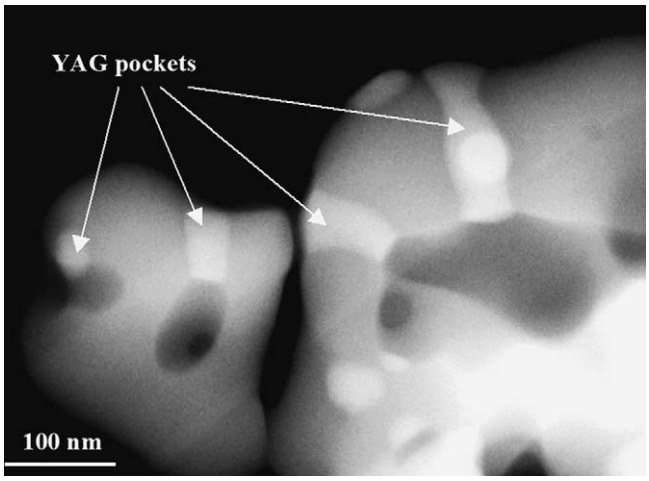

Fig. 7. HAADF image of AY-5 calcined at 1300 °C.

4. Discussion

4.1. DTA–TG analysis

DTA results clearly evidence the role of yttrium in delaying the metastable to α-alumina crystallization temperature, as

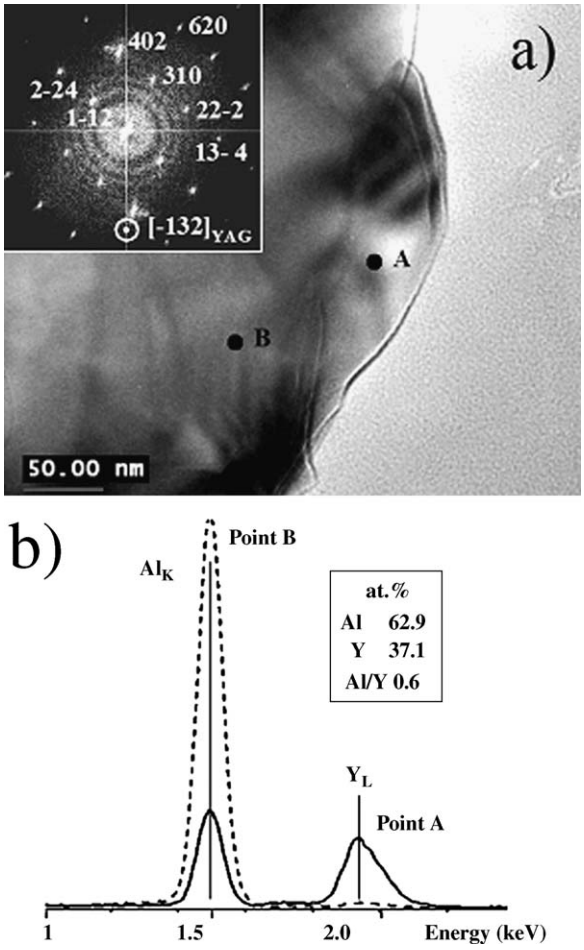

Fig. 8. (a) HRTEM micrograph of AY-5 calcined at 1300 °C (inset to the figure the indexed FFT); (b) EXD spectra in the 1.0–2.5 keV range collected at points A and B of figure (a).

already reported in literature[23–25]; however, despite the numerous investigations, there is not yet a clear understanding of the mechanism responsible for transition alumina thermal stabilization. According to our microstructural observations, we can consider the stabilizing effect of rare-earth cations on the surface of transition Al_2O_3. As proposed by Arai and Machida,[26] such ions can promote the formation of a coherent monolayer of a surface compound (like $LaAlO_3$, in the case of La-doping); the additive cations occupy, in this way, the alumina surface/bulk sites and prevent atomic diffusion which leads to the phase transformation. Further interesting results derive from the recent atomistic simulation study by Maglia et al.[22]: according to these Authors, the incorporation of trivalent ions improves the thermodynamic stability of γ-Al_2O_3 as compared to α-Al_2O_3 due to an enhanced solubility of rare-earth ions in the defect spinel structure of transition alumina in comparison with the corundum one.

4.2. XRD analysis

XRD results highlight two different crystallization trends. Firstly, the higher the yttrium content in the doped powder, the lower the transformed α-alumina fraction (X_α), supporting the previous statements from DTA data on the role of yttrium on the metastable to alpha-alumina transformation. Secondly, the crystallization temperature of yttrium-aluminates decreases by increasing the dopant amount. This result agrees with previous works by Shojaie-Bahaabad et al.[23] and Towata et al.[24], whereas Al-Yassir et al.[25] determined the same crystallization temperature of $YAlO_3$ phase in 2.5–20 wt.% yttria-doped alumina powders.

In addition, the crystallization of YAG involves the formation of h-$YAlO_3$, YAP and YAM as intermediate phases, but different crystallization paths are followed as a function of the starting yttrium content. This result is in partial agreement with some literature data[23,24,27] in which the formation of intermediate hexagonal and orthorhombic $YAlO_3$ phases is observed in alumina–YAG composite powders and fibres produced by sol–gel process. In these works, however, YAM crystallization was never observed, so that differences in phase evolution can be also reasonably imputed to the synthesis route. To explain the formation of intermediate phases prior to YAG, it was argued that the garnet structure was difficult to nucleate as compared to $YAlO_3$, as reported by Li and Gao[28] on the ground of reaction volume change in the θ-Al_2O_3–Y_2O_3 system and related strain energy. If the solidification behavior of YAG from its melt is considered,[20,29] it was also supposed a hard nucleation of the garnet structure due to its complex crystalline structure, made of 160 atoms per unit cell. Such condition makes difficult the germination of YAG nuclei with radius larger than the critical size required for the crystallites growth, thus promoting the creation of the simpler $YAlO_3$ structure with only 20 atoms per unit cell.

4.3. HRTEM characterization

4.3.1. Low-temperature treatments

HRTEM data of AY-5 calcined in this temperature range confirmed the XRD results presented in Table 1. Precisely, only transition alumina phases are here present, whereas yttria or yttrium-aluminates particles did not crystallize, due to a negligible diffusion of yttrium from alumina surface to bulk up to 1150 °C. In a previous work[30] yttrium bulk diffusion in α-alumina single crystal was estimated at this temperature: the Authors report a mean penetration depths of yttrium into alumina of 35 nm and a bulk diffusion coefficient of $2.5 \times 10^{-8}\ m^2\ s^{-1}$ after 135 h of annealing at 1150 °C. By comparing our experimental result with this literature datum, similar thermal treatments are now in progress, with the aim of producing different alumina–YAG fired microstructures by inducing the YAG crystallization at lower-temperature but for prolonged times.

A different result was also found by Schehl et al.[9], reporting the formation of very fine yttria precipitates on the surface of α-alumina powders doped with yttrium methoxyethoxide, after calcination at 850 °C for 2 h. This discrepancy can be ascribed to the chemical nature of the precursor which, in that case, probably gives rise to an "in situ sol–gel process", also affecting the phase development and crystallization phenomena upon thermal treatment.

HRTEM characterization also assessed the "complex" phase structure of Nanotek® alumina, probably made by both δ-Al_20_3 (in agreement with the supplier data sheet[16]) and δ*-Al_20_3 (according with our XRD results[17]) phases. In fact, the FFT of an alumina particle of as-dried AY-5 is well indexed with δ-Al_20_3, whereas in the powder calcined at 1150 °C the proposed indexation allows to identify the δ*-phase. More precisely, such indexation corresponds to the best coherent appellation for the spots, compared to those related to other possible phases, so-called transition alumina, following the crystallisation sequence γ, δ, η, θ alumina[31] (all them have a face-centered cubic arrangement of oxygen atoms). The indexation work was carried out according to the following crystallographic features and lattice parameters for the different structures of γ or δ-Al_2O_3 phases.

The crystallography of γ-phase corresponds to a $Fd-3m$ cubic spinel structure, with slightly different lattice parameter on the ground of the related JCPDFS files (50-741 or 47-1292). Several propositions exist, indeed, for the diffraction data of δ-phase: JCPDS file 46-1131 gives the lattice parameters for a $P-4m2$ tetragonal structure; file 46-1215 indicates an orthorhombic structure, here notified as δ*: P222 while file 47-1770 supplies the lattice parameters according to a tetragonal structure, here notified as δ′. Concerning the θ-phase, file 35-121 indicates an $A2/m$ monoclinic structure while data given in file 11-517 correspond to a surstructure of previous phase. The structure of δ alumina is close to that of γ: in terms of lattice description, exist the vectorial relations: $\mathbf{a}_\delta \approx (1/2)\mathbf{a}_\gamma + (1/2)\mathbf{b}_\gamma$; $\mathbf{b}_\delta \approx -(1/2)\mathbf{a}_\gamma + (1/2)\mathbf{b}_\gamma$ (due to $a_\gamma \approx \sqrt{2}\cdot a_\delta$) and $\mathbf{c}_\delta \approx 3\mathbf{c}_\gamma$. So, these relations lead to a correspondence between the Miller $h\,k\,l$ indices of the two phases: $h_\delta \approx (1/2)(h_\gamma + k_\gamma)$; $k_\delta \approx (1/2)(-h_\gamma + k_\gamma)$ and $l_\delta \approx 3l_\gamma$. For instance, the (1 1 1) diffraction line of γ alumina is similar to (1 0 3) line of δ phase. We see of course that Miller indices l_δ which are not a multiple of 3 have not signification in the γ-alumina lattice. Here is a possibility to distinguish between the two phases. Now, the correspondence between γ and δ* lat-

tices is still more simple. If we except the small orthorhombic distortion, we have: $\mathbf{a}_{\delta^*} \approx \mathbf{a}_\gamma$; $\mathbf{b}_{\delta^*} \approx \mathbf{b}_\gamma$ and $2\mathbf{c}_{\delta^*} \approx 3\mathbf{c}_\gamma$. So, the Miller indices $(h_\gamma\, k_\gamma\, l_\gamma)$ in γ phase correspond to $(h_\gamma\, k_\gamma\, 3/2l_\gamma)$ in δ* which is applied only when l_γ is odd. For the case of δ′ alumina, similarly to the previous one, we have $\mathbf{a}_{\delta'} \approx \mathbf{a}_\gamma$; $\mathbf{b}_{\delta'} \approx \mathbf{b}_\gamma$ and $\mathbf{c}_{\delta'} \approx 3\mathbf{c}_\gamma$ giving a transposition between Miller indices: $(h_\gamma\, k_\gamma\, l_\gamma)$ in $\gamma \rightarrow (h_\gamma\, k_\gamma\, 3l_\gamma)$ in δ′. All mentioned restrictive conditions are useful to choose between the four phases γ, δ, δ*or δ′ during indexation work of electron diffraction patterns and FFT of HRTEM micrographs.

4.3.2. High-temperature treatments

The change in the alumina particles morphology, from mainly spherical to facetted shape, can be the result of a diffusion process leading to develop the natural faces of crystals, i.e. having a lowest surface energy. In addition, the primary alumina particles are here found in form of aggregates: as expected, the higher calcination temperature induced their partial sintering. On the contrary, to the best of the Author's knowledge, the formation of yttrium-rich films, quite "sticking" the alumina grains each other, was never reported before in literature for materials in the alumina–yttria system. This phenomenon can represent the first step toward yttrium–aluminates crystallization and alumina–YAG composite development, as described in the followings.

Differently from these yttrium-enriched films, the structural lattice defects inside alumina grains, when observed, (see Fig. 5(b)) were apparently completely yttrium-free on the base of EDX nanoprobe measurements. At higher magnification (Fig. 9(a)), this defect appears to act as a mirror plane between twin grains. The respective FFT in Fig. 9(b) shows spot splitting, obtained from the two differently orientated domains, allowing to determine the twin relationship. Precisely, spots allow to associate the cubic γ-Al_2O_3 phase to both grains, being the twin crystal II rotated by 60° compared to grain I. The twin relationship can be defined as $\Sigma 3$, where Σ is the inverse density of coincidence lattice sites in the matrix and in the twin lattice.[32] A previous work by Swiatnicki et al.[33] reported that this coherent grain boundary was not affected by yttrium segregation in Y-doped alumina sintered materials, arguing that one-third of the atomic sites of the twin boundary were common to the twin grains, thus limiting the number of foreign atoms hosted in this region. In contrast, Buban et al.[34] attested the presence of yttrium in $\Sigma 31$ grain boundaries by using Z-contrast images. Their results suggest that Y^{3+} simply replaces Al^{3+} at specific sublattice cation sites and drastically changes the chemical bonds state of the surrounding atoms (precisely form ionic-type bonding in pure alumina to covalent-type in doped samples), with the important effect of improving the grain boundary strength.

Finally, in this temperature range yttrium-aluminates second-phases are detected, according to XRD data, and a tentative explanation of the whole crystallization mechanism is here proposed. (Step 1) After doping, a continuous yttrium-rich thin layer is formed on the alumina particles surface, as demonstrated by systematic nanoprobe EDX analyses. Such homogenous coating, few nanometer thick, is detectable exclusively on the alumina grain surface up to 1150 °C. (Step 2) Starting from

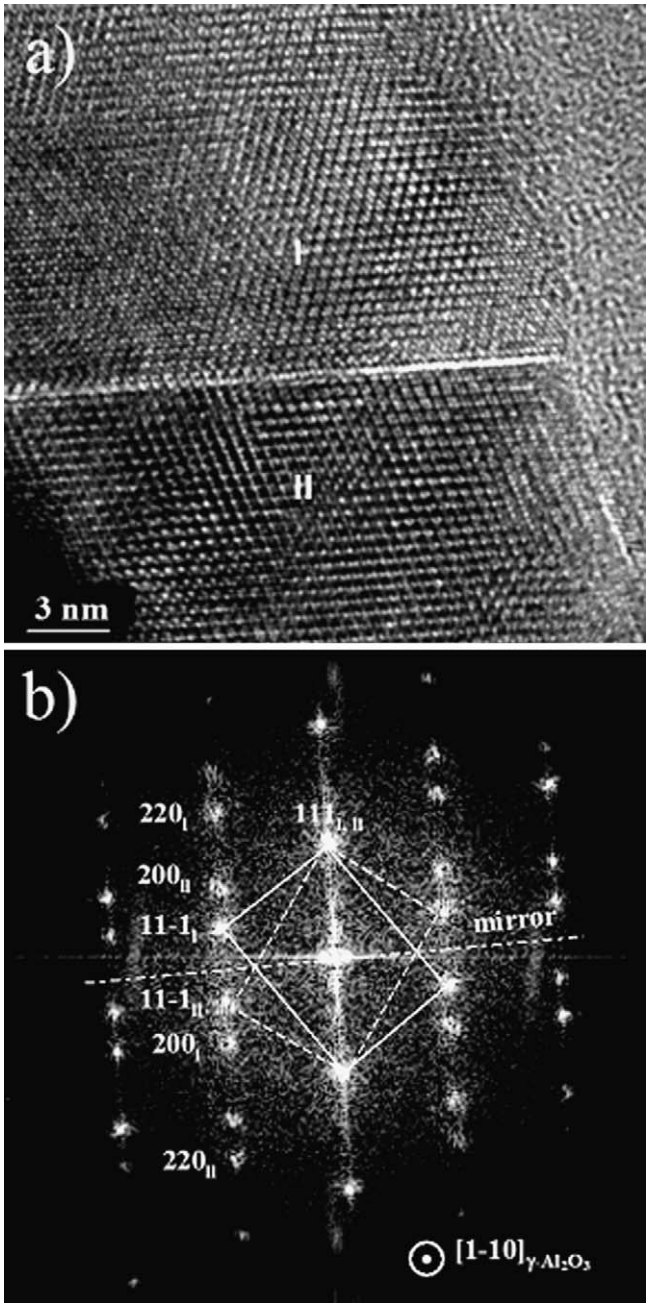

Fig. 9. (a) High magnification HRTEM image of interfacial region between domains I and II of Fig. 5(b); (b) γ-alumina indexed diffraction spots from FFT of figure (a) where the two domains exhibit a {1 1 1} mirror orientation.

1200 °C, the metastable alumina grains start to transform into α-Al_2O_3 and aggregates of primary particles are formed. (Step 3) As a consequence of the increased atomic mobility (due to the higher temperatures here involved), the yttrium enrichment is produced at the contact points between the alumina particles. Such a mechanism could be assisted by a decreased yttrium solubility into the alumina lattice, as stated by literature.[24] (Step 4) At even higher calcination temperature, aggregates of partially sintered alumina particles continue to form, inducing further yttrium enrichment at alumina grain boundaries or at the triple joints, leading to the final precipitation of yttrium-aluminates,

yielded by solid-state reaction with alumina,. This explanation is supported by the microstructural observation which shows second-phase grains preferentially located on the alumina surface, whereas intra-granular crystallization was rarely detected.

5. Conclusions

In this paper, yttrium-doped nanocrystalline transition alumina powders are characterized by XRD, DTA and high spatial resolution microscopy techniques. Our aim is to follow the phase and microstructural evolution of the powders thermally treated in a wide temperature range (from as-dried at 105° to calcined at 1500 °C), toward the formation of alumina–YAG composite materials.

It is found that both alumina and yttrium-aluminates crystallization paths are significantly affected by the yttrium content. In fact, yttrium-doped materials present a delayed metastable to α-alumina transition as compared to the pure powder; in addition, the higher the yttrium content, the higher the metastable to α-alumina transformation temperature but the lower the crystallization temperature of yttrium-containing phases.

By HRTEM observations coupled with systematic nanoprobe EDX analyses, carried out on the particles surface and bulk, we can assert that the doping process can successfully induce the formation of a homogenous and thin (few nanometers in thickness) yttrium-rich layer on the alumina particles surface. Such layer is stable with the temperature and no yttrium diffusion inside the alumina bulk particles is evidenced up to 1150 °C. Starting from 1200 °C, some major morphological, crystallographic and compositional changes occur: the α-Al_2O_3 phase transformation is accompanied by the formation of aggregates of partially sintered alumina grains. On the ground of these observations, a tentative explanation of the yttrium-aluminates crystallization mechanism is proposed.

Finally, this work demonstrated to be a powerful tool for a better exploitation of the innovative processing route set-up for the production of alumina–YAG micro/nano-composite materials. For instance, the information concerning the yttrium diffusion thermal conditions as well as the identification of the thermal treatment which brings to hard-agglomerates, crucial for the composite powder sintering, are of great importance for a more conscious tailoring of the final microstructures.

References

1. Sathiyakumar M, Gnanam FD. Influence of additives on density, microstructure and mechanical properties of alumina. *J Mater Process Technol* 2003;**133**:282–6.
2. Voyotovych R, MacLaren I, Gulgun MA, Cannon RM, Ruhle M. The effect of yttrium on densification and grain growth in α-alumina. *Acta Mater* 2002;**50**:3453–534.
3. Bae SI, Baik S. Critical concentration of MgO for the prevention of abnormal grain growth in alumina. *J Am Ceram Soc* 1994;**77**:2405–99.
4. Lartigue S, Priester L, Dupau F, Gruffel P, Carry C. Dislocation activity and differences between tensile and compressive creep of yttria-doped alumina. *Mater Sci Eng A* 1993;**164**:211–5.
5. Cho J, Harmer MP, Chan HM, Rickman JM, Thompson AM. Effect of yttrium and lanthanum on tensile creep behaviour of aluminum oxide. *J Am Ceram Soc* 1997;**80**:1013–7.
6. Lartigue-Korinek S, Carry C, Priester L. Multiscale aspects of the influence of yttrium on microstructure, sintering and creep of alumina. *J Am Ceram Soc* 2002;**22**:1525–41.
7. Wang CM, Cargill III GS, Chan HM, Harmer MP. Structural features of Y-saturated and supersaturated grain boundaries in alumina. *Acta Mater* 2000;**48**:2579–91.
8. Torrecillas R, Schehl M, Diaz LA, Menendez JL, Moya JS. Creep behaviour of alumina/YAG nanocomposites obtained by a colloidal processing route. *J Eur Ceram Soc* 2007;**27**:143–50.
9. Schehl M, Diaz LA, Torrecillas R. Alumina noncomposites form powder-alkoxide mixtures. *Acta Mater* 2002;**50**:1125–39.
10. French JD, Zhao J, Harmer MP, Chan HM, Miller GA. Creep of duplex microstructures. *J Am Ceram Soc* 1994;**77**:2857–65.
11. Duong H, Wolfestine J. Creep behaviour of fine-grained two-phase Al_2O_3–$Y_3Al_5O_{12}$ materials. *Mater Sci Eng A* 1993;**172**:173–9.
12. Tai Q, Mocellin A. Review: High temperature deformation of Al_2O_3-based ceramic particle or whisker composites. *Ceram Int* 1999;**25**:395–408.
13. Palmero P, Naglieri V, Chevalier J, Fantozzi G, Montanaro L. Alumina-based nanocomposites obtained by doping with inorganic salt solutions: application to immiscible and reactive systems. *J Eur Ceram Soc* 2009;**29**:56–66.
14. Naglieri V, Palmero P, Montanaro L. Preparation and characterization of alumina-doped powders for the design of multi-phasic nano-microcomposites. *J Therm Anal Calorim* 2009;**97**:231–7.
15. Cinibulk MK. Effect of yttria and yttrium–aluminum garnet on densification and grain growth of alumina at 1200–1300 °C. *J Am Ceram Soc* 2004;**87**:692–5.
16. http://www.nanophase.com.
17. Palmero P, Lombardi M, Montanaro L. Effect of heating rate on phase and microstructural evolution during pressureless sintering of a nanostructured transition alumina. *Int J Appl Ceram Technol* 2009;**6**:420–30.
18. Fargeot D, Mercurio D, Dauger A. Structural characterization of alumina metastable phases in plasma sprayed deposits. *Mater Chem Phys* 1990;**24**:299–314.
19. Azar M, Palmero P, Lombardi M, Garnier V, Montanaro L, Fantozzi G, et al. Effect of initial particle packing on the sintering of nanostructured transition alumina. *J Eur Ceram Soc* 2008;**28**:1121–8.
20. Cockayne B. The use and enigmas of the Al_2O_3–Y_2O_3 phase system. *J Less-Common Met* 1985;**114**:199–206.
21. Bonelli B, Palmero P, Pomello F, Armandi M, Lombardi L. Study of the effect of prolonged magnetic stirring on the physico-chemical surface properties of nanometric transition alumina. *J Mater Sci* 2010;**45**:6115–25.
22. Maglia F, Gennari S, Buscaglia V. Energetics of aluminum vacancies and incorporation of foreign trivalent ions in α-Al_2O_3: an atomistic simulation study. *J Am Ceram Soc* 2008;**91**:283–90.
23. Shojaie-Bahaabad M, Taheri-Nassaj E, Naghizadeh R. Effect of yttria on crystallization and microstructure of an alumina–YAG fiber prepared by aqueous sol–gel process. *Ceram Int* 2009;**35**:391–6.
24. Towata A, Hwang HJ, Yasuoka M, Sando M, Niihara K. Preparation of polycrystalline YAG/alumina composite fibers and YAG fiber by sol–gel method. *Compos Part A* 2001;**32**:1127–2113.
25. Al-Yassir N, Le Van Mao R. Thermal stability of alumina aerogel doped with yttrium oxide, used as a catalyst support for the thermocatalytic cracking (TCC) process: an investigation of its textural and structural properties. *Appl Catal A-Gen* 2007;**317**:275–83.
26. Arai H, Machida M. Thermal stabilization of catalyst supports and their application to high-temperature catalytic combustion. *Appl Catal A-Gen* 1996;**138**:161–76.
27. Hassanzadeh-Tabrizi SA, Taheri-Nassaj E. Compressability and sinterability of Al_2O_3–YAG nanocomposite powder synthesized by an aqueous sol–gel method. *J Alloy Compd* 2010;**506**:640–4.
28. Li WQ, Gao L. Co-precipitation processed needle-like YAG dispersed in alumina powder. *Mater Lett* 2001;**48**:157–61.
29. Jaroslav L, Casalavsky L, Viechnicki J. Melting behaviour and metastability of yttrium aluminum garnet (YAG) and $YAlO_3$ determinated by optical differential thermal analysis. *J Mater Sci* 1980;**15**:1709–18.
30. Moya EG, Moya F, Lesage B, Loudjani MK, Grattepain C. Yttrium diffusion into α-alumina single crystal. *J Eur Ceram Soc* 1998;**18**:591–4.

31. Bumaza A, Favaro L, Lédion J, Sattonnay G, Brubach JB, Berthet D, et al. Transition alumina phases induced by heat treatment of boehmite: an X-ray diffraction and infrared spectroscopy study. *J Solid State Chem* 2009;**182**:1171–6.
32. Kaplan WD, Kenway PR, Brandon DG. Polymorphic basal twin boundaries and anisotropic growth in α-Al_2O_3. *Acta Metall Mater* 1995;**43**:835–49.
33. Swiatnicki W, Lartigue-Korinek S, Laval JY. Grain boundary structure and intergranular segregation in Al_2O_3. *Acta Metall Mater* 1995;**43**:795–805.
34. Buban JP, Matsunaga K, Chen J, Shibata N, Ching WY, Yamamoto T, et al. Grain boundary strengthening in alumina by rare earth impurities. *Science* 2006;**311**:212–5.